Structural insight into the magnesium borohydride – ethylenediamine solid-state Mg-ion electrolyte system†

Igor E. Golub, [a] Michael Heere,*[b,c] Volodia Gounaris,[a] Xiao Li,[a] Timothy Steenhaut, [a] Jian Wang,[a] Koen Robeyns, [a] Hai-Wen Li,[d] Iurii Dovgaliuk, [e,f] Kazutaka Ikeda, [g] Geoffroy Hautier [a] and Yaroslav Filinchuk*[a]

A highly complex crystal structure of stoichiometric $Mg_5(en)_6(BH_4)_{10}$ was solved from single crystal synchrotron X-ray diffraction and confirmed by neutron powder diffraction (NPD) on isotopically substituted $Mg(en)_{1.2}(^{11}BD_4)_2$. We highlight the role of the amorphous $Mg(BH_4)_2$ in the reactivity of the $Mg(BH_4)_2$-*en* system and characterized a previously overlooked phase, $Mg(en)_2(BH_4)_2$.

Introduction

Development of "beyond Li-battery" applications, such as Na, Mg or Ca-batteries, for electrochemical storage of energy is one of the grand challenges for our generation of researchers. Over recent years, the energy production from renewables has increased worldwide, resulting in a higher demand for suitable energy storage systems. Currently, those span from chemical to physical and electrochemical storage systems. Among other energy storage technologies, "beyond Li-batteries" with alternative working ions include, but are not limited to, Na^+, Mg^{2+}, and Ca^{2+}, which are considered as cheaper and more abundant. Furthermore, with bivalent ions, a potentially higher energy density is achievable compared to the current state of the art technology, mainly based on Li-ion batteries. Nevertheless, the transport properties in solid-state electrolytes based on double-charged Mg^{2+} are challenging and directly correlated to the underlying crystal structure.

[a]*Institute of Condensed Matter and Nanosciences (IMCN), Université catholique de Louvain (UCLouvain), 1348 Louvain-la-Neuve, Belgium. E-mail: m.heere@tu-bs.de, yaroslav.filinchuk@uclouvain.be*

[b]*Institute for Applied Materials—Energy Storage Systems (IAM-ESS), Karlsruhe Institute of Technology (KIT), 76344 Eggenstein, Germany*

[c]*Technische Universität Braunschweig, Institute of Internal Combustion Engines, Hermann-Blenk-Straße 42, 38108 Braunschweig, Germany*

[d]*Hefei General Machinery Research Institute (HGMRI), Hefei 230031, China*

[e]*Swiss–Norwegian Beamlines, European Synchrotron Radiation Facility, 71 Rue des Martyrs, Grenoble, 38043, France*

[f]*Institut des Matériaux Poreux de Paris, Ecole Normale Supérieure, ESPCI Paris, CNRS, PSL Université, 75005 Paris, France*

[g]*Institute of Materials Structure Science, High Energy Acelerator Research Organization (KEK), Tsukuba, Ibaraki 305-0801, Japan*

Mg-ion batteries (MIBs) have several advantages compared to Li-ion technology.[1,2] For instance, the −2.4 V electrochemical potential of Mg/Mg^{2+} [*vs.* standard hydrogen electrode (SHE)] is close to the one of Li/Li^+ (−3.0 V), which enables high cell voltages. Furthermore, Metallic Mg has a higher volumetric capacity of 3.833 mA h cm ^{3} compared to 2.036 mA h cm ^{3} for Li metal, and Mg is found in higher abundancy (about 2%) in the Earth's crust (compared to 0.006% for Li).[2] In addition, Mg is beneficial due to its non-toxicity, easy machining and handling properties.[3,4] Although a recent study suggests the appearance of dendrites,[5] magnesium is much less prone to their formation than Li,[6] for which hazardous Li plating is a major safety concern. Thus, 'pure' Mg metal, with a very high capacity, could be used as safer and more reliable anode material.

A "renaissance as energy materials" was attested for the research on complex metal hydrides by Mohtadi and Orimo in 2017.[7] Since then, Mg-electrolyte research can be divided into the liquid and the solid-state directions. Mohtadi *et al.* were the first to develop a liquid electrolyte based on magnesium borohydride (for a more general review on borohydrides see ref. 8). Their study demonstrated a secondary magnesium battery and employed $Mg(BH_4)_2$ dissolved in tetrahydrofuran (THF) and dimethoxyethane (DME).[9] Thereafter, $Mg(BH_4)_2$ was replaced by $Mg[B(OCH(CF_3)_2]$ in DME. This complex shows the highest reported electrochemical stability window yet, being 4.3 V. Furthermore, it is stable in air and a Mg-ion conductivity (σ) of 0.011 S cm ^{1} was measured in a 0.3 M solution in DME.[10]

The second direction (solid-state Mg-ion conductors) is receiving more and more attention. Roedern *et al.* synthesized a new compound from $Mg(BH_4)_2$ and ethylenediamine ($H_2N(CH_2)_2NH_2$, '*en*'), which at that point, had the highest reported Mg-ion conductivity (up to 6×10^{5} S cm ^{1} at 343 K).[11] The

synthesis was solely based on mechanochemical milling techniques followed by an additional thermal treatment.[12] Nevertheless, the structure of their "$Mg(en)_1(BH_4)_2$" has not been reported, while the stoichiometry was based on phase analysis of samples from different reactant ratios. Since then, other solvated derivatives were reported with the $Mg(BH_4)_2$ precursor, such as a mixture with diglyme, having reported conductivities of 2×10^{-5} S cm^{-1} at 350 K for $Mg(diglyme)_{0.5}(BH_4)_2$.[13] Even earlier, $Mg(NH_2)(BH_4)$ was reported to be a good solid-state Mg ion conductor,[14] while more recently a conductivity of 4×10^{-5} S cm^{-1} at 373 K and the reversible Mg deposition/stripping were reported for $Mg_3(NH_2)_2(BH_4)_4$.[15]

A pioneering work has recently been published by Jensen *et al.*, who even reported a conductivity of 3.3×10^{-4} S cm^{-1} at 353 K for $Mg(BH_4)_2{\cdot}NH_3$.[16] In connection with an earlier work[17] they suggested a new approach based on NH_3 dynamics to explain the conductivity in these materials.[16] Other similar systems, like $Mg(BH_4)_2{\cdot}2NH_3BH_3$ also show high conductivity.[18,19] In general, the amount of work on Mg conductors, and notably M–B–N–H systems (M = Li, Mg), seems to increase.[16,20–23] With that motivation, the present work addresses the structural characterization of a Mg-ion conductor, described in literature as "$Mg(en)(BH_4)_2$".

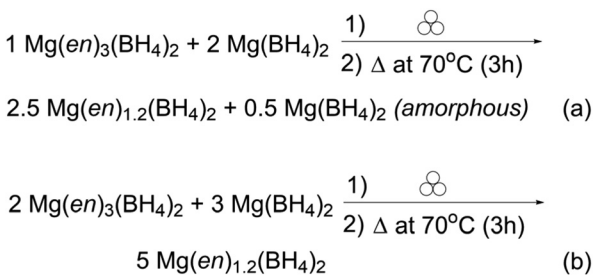

Scheme 1 Synthesis of $Mg(en)_{1.2}(BH_4)_2$ by ball-milling with subsequent annealing.

Results and discussion

We carried out the synthesis of "$Mg(en)(BH_4)_2$" according to Scheme 1(a), which actually results in the formation of Mg $(en)_{1.2}(BH_4)_2$ (see the structural characterization below) and amorphous $Mg(BH_4)_2$. Our structural study shows that the true composition of the phase in question is $Mg_5(en)_6(BH_4)_{10}$, *e.g.* having a 5 : 6 stoichiometric ratio of Mg to *en*. Its crystal structure shows an unprecedented complexity, and its determination may open the way to understanding the mechanism of Mg diffusion in this solid. The conducting samples of "Mg $(en)_1(BH_4)_2$" thus contain an excess of γ-$Mg(BH_4)_2$, which is likely turned into an X-ray amorphous phase.[24,25] We report the new synthetic procedures for $Mg(en)_{1.2}(BH_4)_2$, phase transformations induced by heat, as well as the new compound Mg $(en)_2(BH_4)_2$ and its crystal structure forming in a magnesium borohydride – ethylenediamine system. All this information is needed for the better understanding the future of solid-state conductors based on $Mg(BH_4)_2$ and organic ligands. Furthermore, it is also a basis for the study of dynamics in Mg $(en)_{1.2}(BH_4)_2$ by quasi-elastic neutron scattering (QENS) and nuclear magnetic resonance (NMR) spin–lattice relaxation measurements that are currently under way.

The diffraction patterns obtained by *in situ* synchrotron radiation X-ray powder diffraction (SR-XRPD) from room temperature (RT) up to the decomposition (Fig. 1) are similar to those reported by Roedern*et al.*,[11] including the Bragg peaks (stronger peaks at Q ~1.10 Å^{-1} and ~1.27 Å^{-1}), which we attribute to an impurity (**I**) phase.

The solid state ^{11}B NMR and attenuated total reflectance infrared (ATR-IR) spectra (Fig. S1 and S2†) are also highly con-

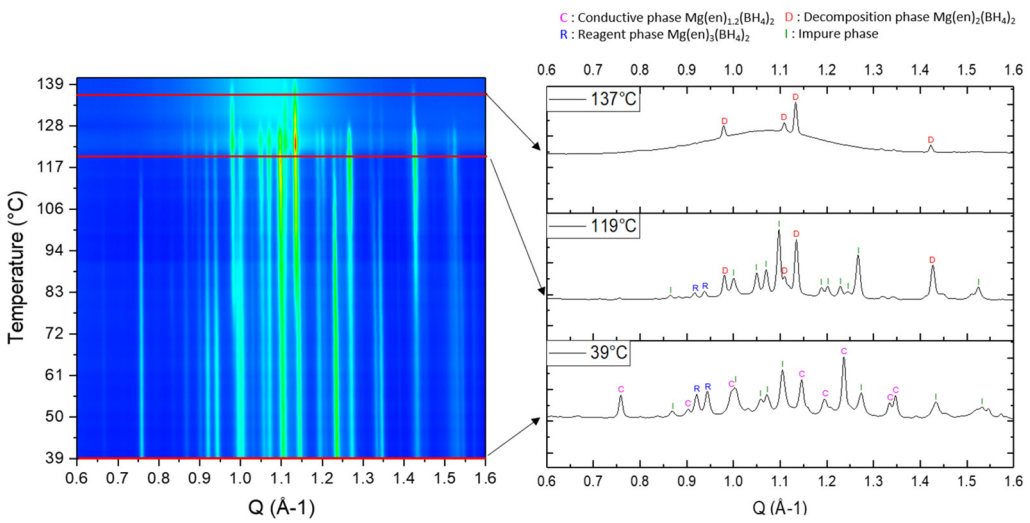

Fig. 1 *In situ* SR-XRPD vs temperature for "$Mg(en)_1(BH_4)_2$" prepared by Scheme 1(a). Besides the main $Mg(en)_{1.2}(BH_4)_2$ phase (**C**), two side products are observed: an impurity (**I**) and the decomposition (**D**) phases. Small amounts of reagents (**R**) typically remain in the samples. Upon heating, first the $Mg(en)_{1.2}(BH_4)_2$ phase decomposes, at higher temperatures only the **D** phase remains crystalline.

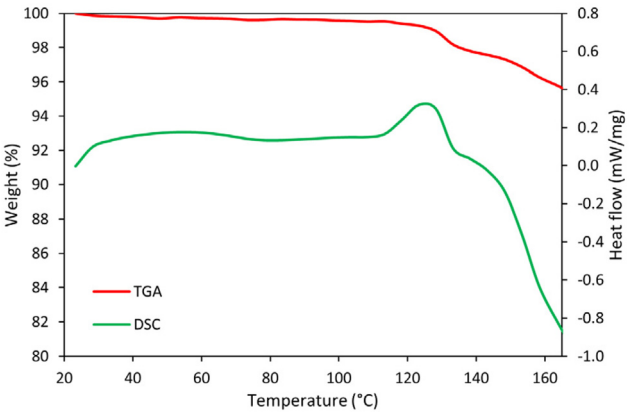

Fig. 2 TGA-DSC curves for the $Mg(en)_{1.2}(BH_4)_2$ sample prepared according to Scheme 1(a). The endothermic decomposition occurs with concomitant weight loss at 123 °C.

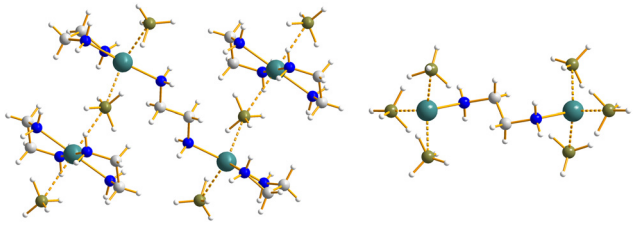

Fig. 3 The crystal structure of $Mg(en)_{1.2}(BH_4)_2$: the cation $[Mg_3(en)_5(BH_4)_4]^{2+}$ constituting the coordination polymer chains $[Mg^{2+}(\kappa^2\text{-}en)_2(\mu_2,\kappa^{1,2}\text{:}\kappa^2\text{-}BH_4^-)Mg^{2+}(\kappa^2\text{-}en)(\kappa^2\text{-}BH_4^-)(\mu_2\text{-}en)Mg^{2+}(\kappa^2\text{-}en)(\kappa^2\text{-}BH_4^-)(\mu_2,\kappa^2\text{:}\kappa^{1,2}\text{-}BH_4^-)]$ (left) and the isolated binuclear anion $[\{Mg(\kappa^3\text{-}BH_4)(\kappa^2\text{-}BH_4)_2\}_2(\mu_2\text{-}en)]^{2-}$ (right). Colour scheme: Mg (aquamarine), N (blue), B(olive), C (grey), H (white).

sistent with the published ones.[11] However our thermogravimetric analysis coupled with differential scanning calorimetry (TGA-DSC) shows that the "$Mg(en)_1(BH_4)_2$" phase decomposes at 123 °C (see Fig. 2), which is considerably higher than the 75 °C reported in ref. 11. At 137 °C, the decomposition phase, marked **D** in Fig. 1, remains the only crystalline product. Below we will show that it corresponds to the previously unknown phase, $Mg(en)_2(BH_4)_2$.

We have made numerous unsuccessful attempts to solve the crystal structure of the main phase from high-resolution X-ray powder diffraction data. Finally, the sample with the nominal composition "$Mg(en)_1(BH_4)_2$" was annealed at 70 °C for 3 hours yielding crystals of about 20 microns, which is a sufficient size for structure determination using synchrotron radiation. Although the 1 : 1 metal to *en* ratio is the most intuitive, similar to other complexes with N-donor ligands, like $Mg(TMEDA)_1(BH_4)_2$,[26] the true composition of this conductive phase reveals to be $Mg(en)_{1.2}(BH_4)_2$, namely the full stoichiometric $Mg_5(en)_6(BH_4)_{10}$. The crystal structure of $Mg(en)_{1.2}(BH_4)_2$ is triclinic, space group $P\bar{1}$. It contains four crystallographically independent *en* molecules and five BH_4 groups. Strikingly, Mg atoms show three different coordination numbers of 4, 5 and 6 (Fig. 3). It is composed of a polymeric chain-like complex cation (Fig. 3, left), $[Mg_3(en)_5(BH_4)_4]^{2+}$, charge-balanced by isolated binuclear complex anions, $[Mg_2(en)(BH_4)_6]^{2}$ (Fig. 3, right). Detailed description of the crystal structure of $Mg(en)_{1.2}(BH_4)_2$, including the B–H···H–N dihydrogen bonds of 2.04–2.36 Å that are apparently playing an important role in Mg ion conductivity,[14] is given in Table S1 in the ESI.†

The organic and inorganic ligands, namely *en* and BH_4, are playing various roles as bridging and terminal ligands. Ethylenediamine plays a role as both chelating (in the cation) and bridging (in the cation and the anion) ligands. Regarding the borohydrides, in the cation, the bridging $\mu_2,\kappa^{1,2}\text{:}\kappa^1\text{-}BH_4$ ligand[27] is connecting two Mg atoms, and the terminal $\kappa^2\text{-}BH_4$ is coordinating to one Mg atom. In the anion, both terminal $\kappa^2\text{-}BH_4$ and $\kappa^3\text{-}BH_4$ are present (coordination *via* an edge and a face of the tetrahedron). Thus, the ligands realize all their potential in terms of coordination modes. Such a diversity makes structure solution from X-ray powder diffraction virtually impossible, as it requires reasonable assumptions on the coordination modes and on the number of independent units.[28,29]

Strikingly, the $Mg(en)_{1.2}(BH_4)_2$ structure is not densely packed: a search for voids in Platon[30] with the probe of 0.9 Å radius reveals two small voids accounting for almost 3% of the structure volume. Fig. S3† shows the perspective view of the structure including the two empty voids. Porous borohydrides are a rare occurrence,[31,32] being a testimony to the directional metal–ligand interactions, and here the structure is not densely packed despite its high complexity that usually accounts for all the stereochemical preferences of the constituents. The voids may be instrumental to the Mg ion conductivity, as they can make part of the Mg^{2+} diffusion path.

Neutron powder diffraction (NPD) data was collected at the NOVA instrument at J-PARC, Japan, with a sample of the following nominal composition: "$Mg(H_2N(CH_2)_2NH_2)_1(^{11}BD_4)_2$". The sample was labelled with ^{11}B and deuterium was used instead of ^1H on the borohydride; *en* was used with natural isotopes. This experiment was originally aiming at solving the crystal structure from the combination of the XRPD and NPD data.[33] However, once the structure was solved from a single crystal, we successfully used the obtained model to fit to the NPD data (Fig. 4). The Rietveld refinement with the TOF data, performed in GSAS2,[34] shows that the sample mainly contains only one crystalline phase, with barely visible impurities (the minor Bragg peaks, which are shown in the differential curve are at 1.10 and 1.45 Å $^{-1}$, which agree with those found for the impurity phase (**I**) in Fig. 1), in full accordance with the single crystal structure determination. The weighted profile *R*-factor R_{wp} is 0.556%.

Various synthetic attempts for obtaining the pure $Mg(en)_{1.2}(BH_4)_2$ phase yielded samples having slightly different phase compositions. A careful analysis of the *in situ* SR-XRPD enabled us to identify which set of Bragg peaks belongs to each phase. It was found that performing the synthesis under harsh milling conditions (tungsten carbide milling equip-

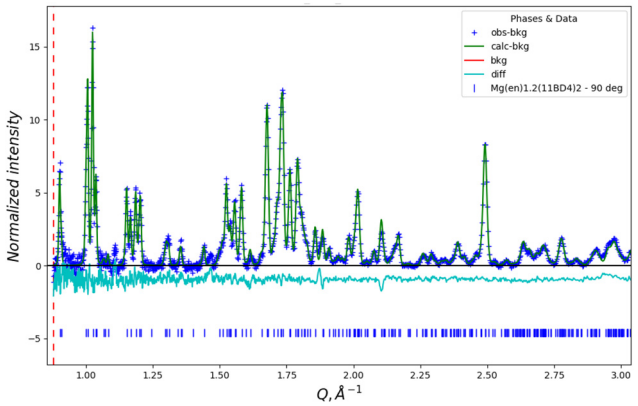

Fig. 4 Rietveld refinement profile, cropped to 3 $Å^{-1}$, for the NPD data collected at the NOVA beamline at J-PARC, Japan. Mg(*en*)$_{1.2}$($^{11}BD_4$)$_2$ was labelled with ^{11}B instead of natural B and deuterium on the borohydride but not on the *en* ligand. The structural model is used from the single crystal synchrotron X-ray diffraction.

ment, ball-to-powder ratio (BPR) of 220–240 : 1) followed by annealing leads, in a reproducible way, to the mentioned impurity phase (**I**), its diffraction pattern is shown on Fig. S4.† To avoid its formation, the synthesis of the samples with the [Mg(*en*)$_3$(BH$_4$)$_2$] : Mg(BH$_4$)$_2$ = 2 : 3 mixture was performed under softer milling conditions (stainless steel milling equipment, BPR of 10–80 : 1). However, even under these conditions, an impurity phase **I** was formed, likely triggered by the temperature increase during milling.

The major phase Mg(*en*)$_{1.2}$(BH$_4$)$_2$, along with the impurity phase, disappears from the diffraction patterns at about 120 °C with the formation of the decomposition phase (**D**, Fig. 1). We used *in situ* synchrotron X-ray powder diffraction data at the nominal temperature of 173 °C to index the Bragg peaks, in the space group $P2_12_12$, and solve the crystal structure. DFT optimization was done on the experimental structure in order to enable better positioning of the light borohydride groups and the final Rietveld refinement (Fig. S6†) was done against the experimental data for the DFT-optimized model.

The decomposition phase (**D**) turns out to have a stoichiometry that was never described before for the magnesium borohydride – ethylenediamine system, namely Mg(*en*)$_2$(BH$_4$)$_2$. Considering that TGA does not detect a significant mass loss (thus no *en* loss to the gas phase), but leads to an increase of the amorphous background upon the formation of Mg(*en*)$_2$(BH$_4$)$_2$, we suggest that the decomposition of Mg(*en*)$_{1.2}$(BH$_4$)$_2$ occurs with the simultaneous formation of Mg(*en*)$_2$(BH$_4$)$_2$ and of the amorphous Mg(BH$_4$)$_2$ (Scheme 2).

$$5\ Mg(en)_{1.2}(BH_4)_2 \xrightarrow{\Delta\ \text{at}\ 120^{\circ}C\ (1h)} 3\ Mg(en)_2(BH_4)_2 + 2\ Mg(BH_4)_2\ (amorphous)$$

Scheme 2 Decomposition reaction for Mg(*en*)$_{1.2}$(BH$_4$)$_2$.

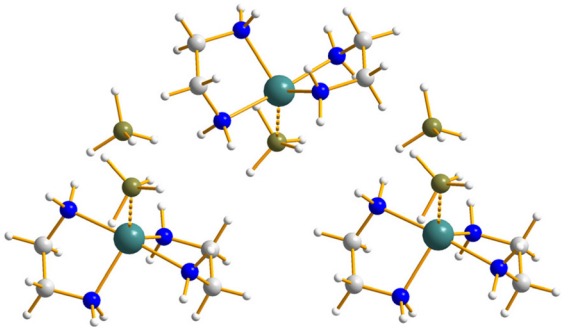

Fig. 5 A fragment of the crystal structure of Mg(*en*)$_2$(BH$_4$)$_2$. Colour scheme: Mg (aquamarine), N (blue), B (olive), C (grey), H (dark grey).

The crystal structure of Mg(*en*)$_2$(BH$_4$)$_2$ is displayed in Fig. 5. It is composed of isolated [Mg(κ^2-*en*)$_2$(κ^2-BH$_4$)]$^+$ cations and BH$_4^-$ anions, linked by dihydrogen bonds of 1.97–2.28 Å (Table S2†).

Systematic study of Mg(BH$_4$)$_2$-*en* system was done by Chen *et al.*,[35] who did not identify the Mg(*en*)$_2$(BH$_4$)$_2$ phase, but their experimental powder patterns for the sample of the nominal composition Mg(BH$_4$)$_2$-2*en* produced powder patterns that we can now interpret as a mixture of Mg(*en*)$_2$(BH$_4$)$_2$ and Mg(*en*)$_3$(BH$_4$)$_2$ phases. We explain this by the presence of the less reactive amorphous Mg(BH$_4$)$_2$ in the starting crystalline γ-Mg(BH$_4$)$_2$ precursor. Since a part of the Mg(BH$_4$)$_2$ did not react with *en*, this resulted in formation of *en*-rich phase.

We found that diffraction-pure Mg(*en*)$_2$(BH$_4$)$_2$ could be obtained by cryomilling using the same ratio of Mg(*en*)$_3$(BH$_4$)$_2$ and Mg(BH$_4$)$_2$ (2 : 3) as for the synthesis of Mg(*en*)$_{1.2}$(BH$_4$)$_2$. Thus, it seems that the formation of the Mg(*en*)$_2$(BH$_4$)$_2$ phase is thermodynamically more favourable, whereas Mg(*en*)$_{1.2}$(BH$_4$)$_2$ is a meta-stable intermediate.

Experimental details

General considerations

All sample manipulations were performed under an atmosphere of dry argon (≥99.999%) in gloveboxes with oxygen and water levels not exceeding 1 ppm. All commercial compounds were used as received without any purification. Ball-milling syntheses were performed with a Fritsch Pulverisette 7 premium line apparatus. Annealing was made in a reactor made of stainless steel Swagelok parts placed in a tubular oven or on a Schlenk line, under dynamic vacuum of an oil pump.

Synthesis of γ-Mg(BH$_4$)$_2$

Magnesium borohydride, γ-Mg(BH$_4$)$_2$, was synthesized from dimethyl sulphide borane complex (CH$_3$)$_2$S·BH$_3$ (Sigma-Aldrich) and di-*n*-butyl magnesium (*n*-Bu)$_2$Mg (1.0 M solution in heptane, Sigma-Aldrich) according to a synthetic procedure as described in ref. 32. In-house X-ray powder diffraction was used to confirm the γ-Mg(BH$_4$)$_2$ sample purity. Volumetric measurements of nitrogen adsorption in this porous phase

allowed to quantify the amount of the amorphous $Mg(BH_4)_2$ phase at 40%.

Synthesis of γ-$Mg(^{11}BD_4)_2$

The same procedure was used as for the compound made of natural isotopes, but starting with $(CH_3)_2S{\cdot}^{11}BD_3$ (Sigma-Aldrich). The resulting sample was crystallographically pure.

Synthesis of $Mg(en)_3(BH_4)_2$

$Mg(en)_3(BH_4)_2$ was obtained by milling $Mg(BH_4)$ with 3.2 equivalents of ethylenediamine *(en*, 99%, Acros Organics*)* using ball-to-powder mass ratio (BPR) 10 : 1 at 300 rpm for 3 periods of 10 min milling time, interrupted by 5 min cooling breaks. The excess of *en* was subsequently evacuated under dynamic vacuum at 120 °C for 1 hour.[11,35,36] In-house X-ray powder diffraction was used to confirm the purity of Mg $(en)_3(BH_4)_2$.

Synthesis of $Mg(en)_{1.2}(BH_4)_2$

The first round of syntheses was performed for a mixture of $[Mg(en)_3(BH_4)_2]$: $Mg(BH_4)_2$ = 1 : 2, as described by Roedern *et al.*[11] for the composition "$Mg(en)_1(BH_4)_2$". Once we determined the crystal structure of the phase in question, namely $Mg(en)_{1.2}(BH_4)_2$, we have prepared a series of samples aiming for the new ratio, starting from the mixture of $[Mg(en)_3(BH_4)_2]$: $Mg(BH_4)_2$ = 2 : 3, see Scheme 1.

The sample for the single crystal X-ray diffraction experiment was obtained from the reaction mixture $[Mg(en)_3(BH_4)_2]$: $Mg(BH_4)_2$ = 1 : 2. Ball milling was conducted with BPR = 60 : 1, using 200 rpm with 9 periods of 2 min milling time, interrupted by 5 min cooling breaks. The freshly milled sample was annealed at 70 °C for 3 hours in a tubular oven, allowing single crystals of about 20 μm, sufficient for structure determination at the synchrotron X-ray source.

The sample for the neutron powder diffraction experiment was obtained in the same way but using doubly isotopically substituted γ-$Mg(^{11}BD_4)_2$ and *en* containing natural isotopes, for the $[Mg(en)_3(^{11}BD_4)_2]$: $Mg(^{11}BD_4)_2$ ratio 1 : 2. The removal of ^{10}B decreases the absorption of the neutron beam, and of ^1H reduces the background coming from the incoherent scattering; "*en*" was not available in a deuterated version.

Several samples aiming for the original composition "Mg $(en)_1(BH_4)_2$" were prepared at BPR of 120–240 : 1 in stainless steel and tungsten carbide milling jars, with milling speeds from 200 to 400 rpm, with and without subsequent annealing. In some cases, we obtained $Mg(en)_{1.2}(BH_4)_2$ as the main crystalline phase already after milling, while annealing significantly improved its diffraction quality. The formation of the crystalline $Mg(en)_{1.2}(BH_4)_2$ can be initiated by seeding the milled sample with the crystalline phase from the previous batch, before annealing. The samples aiming for the true composition $Mg(en)_{1.2}(BH_4)_2$ showed lower success rate, often producing sticky and amorphous samples, which agglomerate and adhere to the surface of the stainless-steel balls and jar walls during ball milling (Fig. 6, a).

Cryomilling is known as a useful technique that can be used for effective homogenisation of sticky compounds.[37] Thus, in order to prevent amorphization, cryomilling of the $[Mg(en)_3(BH_4)_2]$: $Mg(BH_4)_2$ = 2 : 3 mixture at BPR = 10 : 1 (instead of 60 : 1) was used (Fig. 6, b). However, this resulted in the formation of $Mg(en)_2(BH_4)_2$ as major phase.

Synthesis of $Mg(en)_2(BH_4)_2$

This new phase was first detected as a crystalline intermediate during *in situ* powder diffraction study of $Mg(en)_{1.2}(BH_4)_2$. The sample with $Mg(en)_2(BH_4)_2$ as major phase was obtained by cryomilling of $[Mg(en)_3(BH_4)_2]$: $Mg(BH_4)_2$ = 2 : 3 using (BPR) 10 : 1 at 300 rpm for 3 periods of 10 min milling time, interrupted by 5 min cooling breaks. The stainless-steel milling jar was precooled before ball milling for 10 minutes using a ^{i}PrOH-liquid N_2 mixture as cooling bath.

Structure solution and DFT optimization of $Mg(en)_2(BH_4)_2$

The structure was indexed in the orthorhombic unit cell and solved using simulated annealing in FOX,[38] using the data measured at the SNBL/ESRF at 173 °C. An isolated Mg atom, two rigid tetrahedral anions and one flexible *en* defined by a *z*-matrix were optimized by parallel tempering using a number of antibump restraints. Various space groups were tested, converging at the choice of $P2_12_12$. The structure was refined using the Rietveld method in Fullprof.[39] In order to improve the reliability of the localization of the light atoms, the experimentally determined structure was optimized by DFT methods. The first-principles calculations were performed using density functional theory (DFT) as implemented in the Vienna Ab Initio Simulation Package (VASP) code within the projector augmented wave (PAW) method.[40,41] The generalized gradient approximation (GGA) was used for the exchange–correlation functional.[42] A plane wave basis set with a cutoff of 520 eV is employed to describe the electronic wave function. For integration of the Brillouin zone, a primitive cell was used with a 2 × 2 × 2 Monkhorst–Pack *k*-point mesh. The relaxation was performed using the conjugate gradient algorithm with a convergence cutoff of 0.01 eV $Å^{-1}$. Two operations were necessary for the relaxation. At first, only the hydrogen atoms were allowed to move. Then, with the updated hydrogen positions,

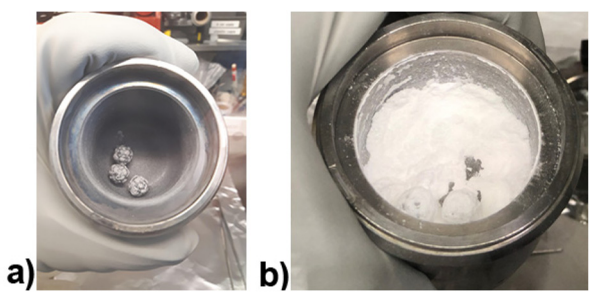

Fig. 6 Photo of stainless-steel jar after ball-milling of $[Mg(en)_3(BH_4)_2]$: $Mg(BH_4)_2$ = 3 : 2 at room temperature at BPR = 60 : 1 (a) and in jar precooled by ^{i}PrOH-liquid N_2 at BPR = 60 : 1 (b).

all the atoms were allowed to move. Symmetrisation was switched off during the whole process. The final Rietveld refinement was done on the DFT optimized structure (Fig. 7), keeping all atomic coordinates fixed, refining only unit cell and profile parameters, along with a small texture along [001] and the overall atomic displacement (in total 10 parameters). The unit cell parameters and discrepancy factors are listed in the caption to the Fig. 7.

Thermogravimetric analysis/differential scanning calorimetry (TGA/DSC)

TGA/DSC analysis was conducted on a Netzsch STA 449 F3 Jupiter instrument contained in an argon-filled glovebox. The experiments were run from room temperature (RT) to 290 °C with a 5 °C min ^{1} heating rate. All measurements were done in Al_2O_3 crucibles. The argon flows (protective and purge gas) were set to 20 and 50 ml min ^{1}, respectively.

Attenuated total reflection fourier-transform infrared spectroscopy (ATR–FTIR)

ATR-FTIR measurements were performed using a Bruker Alpha–Platinum Fourier-Transform Infrared Spectrometer with a diamond crystal inside an Ar-filled glove box. The spectra were measured in the wavenumber range of 4000–400 cm ^{1} with a resolution of 2 cm ^{1} at RT.

In-house powder X-ray diffraction (XRPD)

Laboratory XRPD was performed using a MAR345 diffractometer. The X-ray source was a Rigaku ultraX18 molybdenum rotating anode equipped with a focusing mirror. The samples were packed under argon in glass capillaries of 0.5 mm outer diameter and sealed with wax.

Neutron powder diffraction (NPD)

NPD time-of flight (TOF) data were collected at the NOVA beamline at the Japan Proton Accelerator Research Complex (J-PARC). The sample holder was made of a vanadium cylinder and a null-scattering alloy sample holder made from $V_{96}Ni_4$ alloy. The size of the cylinder was 6 mm in radius, 65 mm in height with a wall thickness of 0.1 mm. The sample holder was inserted in a closed-cycle He refrigerator with He exchange gas, but data were collected at room temperature. The beam size was set to 20 × 20 mm.^{2} All four detector banks were employed with the following configuration: back scattering, 20°, 45° and 90°. The structure was refined by Rietveld methods using GSAS2 software[34] using the model obtained from single crystal synchrotron X-ray diffraction.

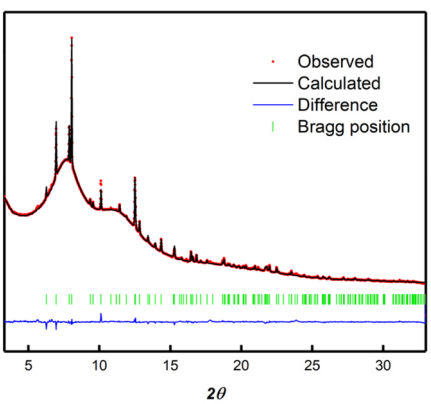

Fig. 7 Rietveld refinement of the Mg(*en*)$_2$(BH$_4$)$_2$ crystal phase at 173 °C. The powder pattern was measured at SNBL/ESRF with a wavelength of 0.77936 Å. R_B = 14.5% (space group $P2_12_12$, a = 9.3580(4), b = 8.8374(4), c = 7.1311(3) Å), R_{wp} = 0.766, χ^2 = 20.

In situ synchrotron radiation X-ray powder diffraction (SR-XRPD)

Measurements were conducted at the Swiss Norwegian Beamlines (SNBL) at the European Synchrotron Radiation Facility (ESRF) in Grenoble, France. The samples were filled in glass capillaries and sealed with wax. Data were collected using a Pilatus 2M detector. The sample–to–detector distances and the wavelength were calibrated from a NIST LaB_6 standard. The exposure time was set to 30 s giving a temperature resolution of 2.5 °C per pattern or 5 °C per pattern and the capillary was rotated by 10° during exposure to improve powder averaging. Both in-house and synchrotron two-dimensional diffraction images were integrated to 1D using the program Fit2D.[43,44]

Single-crystal synchrotron radiation X-ray diffraction

A single crystal was mounted on a glass needle using fluorinated oil and quickly cooled to 100 K under a nitrogen flow of a cryostream from Oxford Cryosystems. Diffraction data were collected with 1 second exposure per frame, 360 frames with a rotation by 1° at the Swiss-Norwegian Beamlines (SNBL) using a Pilatus 2M single-photon counting pixel area detector. These data were processed using the SNBL Toolbox[44] and MEDVED[45] softwares. The recorded data were indexed and integrated with CrysAlisPro, and the implemented absorption correction was applied.[46] A resolution limit of 0.93 Å was imposed, beyond which the crystal diffracted poorly. The structure of Mg(*en*)$_{1.2}$(BH$_4$)$_2$ was solved in the triclinic space group $P\bar{1}$ with a = 7.1569(10) Å, b = 12.192(2) Å, c = 12.5351(17) Å, α = 99.432(13)°, β = 103.986(12)° and γ = 90.464(13)°, by direct methods and refined by full-matrix least squares on F^2 using SHELX2014.[47] R_1 = 9.6%, wR_2 = 21.0% for 238 refined parameters against 2675 independent reflections using 105 restraints.

Solid-state magic angle spinning nuclear magnetic resonance (MAS NMR) spectroscopy

Solid-state MAS NMR spectra were recorded using a Bruker Ascend-600 spectrometer (Bruker, Japan), at RT. NMR sample preparations were always conducted in a glovebox filled with a purified Ar gas and sample spinning was operated using dry N_2 gas. ^{11}B MAS NMR spectra were obtained at excitation pulses of 6.5 μs (π/2 pulse) and with strong ^{1}H decoupling pulses. ^{11}B NMR chemical shifts were referenced to boron trifluoride diethyl etherate $BF_3{\cdot}Et_2O$ (δ = 0.00 ppm).

Conclusions

In this work, a solid-state magnesium ion conductor previously thought to be $Mg(en)_1(BH_4)_2$, was shown to actually be $Mg(en)_{1.2}(BH_4)_2$. The structure of $Mg(en)_{1.2}(BH_4)_2$ was solved from single crystal synchrotron X-ray diffraction in the $P\bar{1}$ space group. The structure was further confirmed by neutron powder diffraction on isotopically substituted $Mg(en)_{1.2}(^{11}BD_4)_2$. Its structure contains three Mg atoms with coordination numbers 4, 5 and 6, with the BH_4 groups behaving as terminal and bridging ligands, and *en* being chelating to and bridging between Mg atoms. This complexity, altogether, makes structure solution from powder diffraction data virtually impossible. Interestingly, the structure is not densely packed and the presence of small voids may be instrumental to Mg ion conductivity, as they can make part of the Mg^{2+} diffusion path. Thermal decomposition of $Mg(en)_{1.2}(BH_4)_2$ goes through the intermediate formation of previously unknown $Mg(en)_2(BH_4)_2$, which structure was solved from synchrotron X-ray powder diffraction, complemented by DFT optimization.

An important conclusion drawn from this work is that control of the crystallinity of magnesium borohydride is important for the reproducibility of results. Indeed, our experiments show that the amorphous fraction of $Mg(BH_4)_2$ is less reactive than the crystalline γ-$Mg(BH_4)_2$. The amorphous part inherently affects ionic conductivity of the samples being omitted in the phase analysis made by X-ray diffraction. One should keep in mind that high-energy ball milling effectively turns γ-$Mg(BH_4)_2$ into the amorphous phase, creating a deficit of the more reactive crystalline phase. This should be considered for other $Mg(BH_4)_2$-based solid state electrolytes, commonly obtained by mechanochemistry.

Author contributions

Project administration, Y. F.; funding acquisition, Y. F. and G. H.; supervision, Y. F., M. H. and G. H., conceptualization, Y. F. and M. H. investigation, I. E. G., M. H., V. G., X. L., T. S. J. W., K. R., H. W. L, I. D. and K. I.; validation, I. G. and V. G.; resources, X. L. and J. W.; visualization, I. G., M. H., T. S., V. G., Y. F. and K. R.; writing—original draft, I. E. G., M. H. and V. G.; writing—review & editing, I. E. G., M. H., T. S., K. R. and Y. F.

Conflicts of interest

There are no conflicts to declare.

Acknowledgements

We acknowledge the beamtime allocation and competent help of BM01 from SNBL at the ESRF, Fédération Wallonie-Bruxelles (ARC 18/23-093 MicroBat), FNRS for FRIA fellowship for TS and EQP and CdR projects (T.0169.13, U.N036.15, U. N022.19, J.0073.20), the China Research Council for CSC fellowships for XL and JW. MH acknowledges the project "Energy Research with Neutrons (ErwiN)",[48] which is funded by the German Federal Ministry of Education and Research (BMBF). The neutron experiment at the Materials and Life Science Experimental Facility of the J-PARC was performed under a user program (Proposal No. 2017B0237).

References

1 S. Payandeh, A. Remhof and C. Battaglia, in *Magnesium Batteries: Research and Applications*, The Royal Society of Chemistry, 2020, pp. 60–78, DOI: **10.1039/9781788016407-00060**.
2 R. Mohtadi, O. Tutusaus, T. S. Arthur, Z. Zhao-Karger and M. Fichtner, *Joule*, 2021, **5**, 581–617.
3 T. D. Gregory, R. J. Hoffman and R. C. Winterton, *J. Electrochem. Soc.*, 1990, **137**, 775–780.
4 D. Aurbach, Y. Cohen and M. Moshkovich, *Electrochem. Solid-State Lett.*, 2001, **4**, A113–A116.
5 R. Davidson, A. Verma, D. Santos, F. Hao, C. Fincher, S. Xiang, J. Van Buskirk, K. Xie, M. Pharr and P. P. Mukherjee, *ACS Energy Lett.*, 2018, **4**, 375–376.
6 M. Jäckle and A. Groß, *J. Chem. Phys.*, 2014, **141**, 174710.
7 R. Mohtadi and S.-i. Orimo, *Nat. Rev. Mater.*, 2016, **2**, 16091.
8 M. Paskevicius, L. H. Jepsen, P. Schouwink, R. Cerny, D. B. Ravnsbaek, Y. Filinchuk, M. Dornheim, F. Besenbacher and T. R. Jensen, *Chem. Soc. Rev.*, 2017, **46**, 1565–1634.
9 R. Mohtadi, M. Matsui, T. S. Arthur and S.-J. Hwang, *Angew. Chem., Int. Ed.*, 2012, **51**, 9780–9783.
10 Z. Zhao-Karger, M. E. G. Bardaji, O. Fuhr and M. Fichtner, *J. Mater. Chem. A*, 2017, **5**, 10815–10820.
11 E. Roedern, R.-S. Kühnel, A. Remhof and C. Battaglia, *Sci. Rep.*, 2017, **7**, 46189.
12 J. Huot, F. Cuevas, S. Deledda, K. Edalati, Y. Filinchuk, T. Grosdidier, B. C. Hauback, M. Heere, T. R. Jensen, M. Latroche and S. Sartori, *Materials*, 2019, 12.
13 T. Burankova, E. Roedern, A. E. Maniadaki, H. Hagemann, D. Rentsch, Z. Lodziana, C. Battaglia, A. Remhof and J. P. Embs, *J. Phys. Chem. Lett.*, 2018, **9**, 6450–6455.
14 S. Higashi, K. Miwa, M. Aoki and K. Takechi, *Chem. Commun.*, 2014, **50**, 1320–1322.
15 R. Le Ruyet, B. Fleutot, R. Berthelot, Y. Benabed, G. Hautier, Y. Filinchuk and R. Janot, *ACS Appl. Energy Mater.*, 2020, **3**, 6093–6097.
16 Y. Yan, W. Dononelli, M. Jørgensen, J. B. Grinderslev, Y.-S. Lee, Y. W. Cho, R. Cerny, B. Hammer and T. R. R. Jensen, *Phys. Chem. Chem. Phys.*, 2020, **22**, 9204–9209.
17 S. Filippov, J. B. Grinderslev, M. S. Andersson, J. Armstrong, M. Karlsson, T. R. Jensen, J. Klarbring, S. I. Simak and U. Häussermann, *J. Phys. Chem. C*, 2019, **123**, 28631–28639.

18 L. H. Jepsen, V. Ban, K. T. Møller, Y.-S. Lee, Y. W. Cho, F. Besenbacher, Y. Filinchuk, J. Skibsted and T. R. Jensen, *J. Phys. Chem. C*, 2014, **118**, 12141–12153.

19 K. Kisu, S. Kim, M. Inukai, H. Oguchi, S. Takagi and S.-i. Orimo, *ACS Appl. Energy Mater.*, 2020, **3**, 3174–3179.

20 Y. Yan, J. B. Grinderslev, Y.-S. Lee, M. Jørgensen, Y. W. Cho, R. Černý and T. R. Jensen, *Chem. Commun.*, 2020, **56**, 3971–3974.

21 A. El Kharbachi, E. M. Dematteis, K. Shinzato, S. C. Stevenson, L. J. Bannenberg, M. Heere, C. Zlotea, P. Á. Szilágyi, J. P. Bonnet, W. Grochala, D. H. Gregory, T. Ichikawa, M. Baricco and B. C. Hauback, *J. Phys. Chem. C*, 2020, **124**, 7599–7607.

22 L. J. Bannenberg, M. Heere, H. Benzidi, J. Montero, E. M. Dematteis, S. Suwarno, T. Jaroń, M. Winny, P. A. Orłowski, W. Wegner, A. Starobrat, K. J. Fijałkowski, W. Grochala, Z. Qian, J. P. Bonnet, I. Nuta, W. Lohstroh, C. Zlotea, O. Mounkachi, F. Cuevas, C. Chatillon, M. Latroche, M. Fichtner, M. Baricco, B. C. Hauback and A. El Kharbachi, *Int. J. Hydrogen Energy*, 2020, **45**, 33687–33730.

23 E. Hadjixenophontos, E. M. Dematteis, N. Berti, A. R. Wołczyk, P. Huen, M. Brighi, T. T. Le, A. Santoru, S. Payandeh, F. Peru, A. H. Dao, Y. Liu and M. Heere, *Inorganics*, 2020, 8.

24 V. Ban, A. V. Soloninin, A. V. Skripov, J. Hadermann, A. Abakumov and Y. Filinchuk, *J. Phys. Chem. C*, 2014, **118**, 23402–23408.

25 M. Heere, A.-L. Hansen, S. Payandeh, N. Aslan, G. Gizer, M. H. Sørby, B. C. Hauback, C. Pistidda, M. Dornheim and W. Lohstroh, *Sci. Rep.*, 2020, **10**, 9080.

26 G. L. Soloveichik, M. Andrus and E. B. Lobkovsky, *Inorg. Chem.*, 2007, **46**, 3790–3791.

27 S. V. Safronov, E. I. Gutsul, I. E. Golub, F. M. Dolgushin, Y. V. Nelubina, O. A. Filippov, L. M. Epstein, A. S. Peregudov, N. V. Belkova and E. S. Shubina, *Dalton Trans.*, 2019, **48**, 12720–12729.

28 D. B. Ravnsbæk, Y. Filinchuk, R. Cerný and T. R. Jensen, *Z. Kristallogr.*, 2010, **225**, 557–569.

29 R. Černý and Y. Filinchuk, *Z. Kristallogr.*, 2011, **226**, 882–891.

30 A. Spek, *Acta Crystallogr., Sect. E: Crystallogr. Commun.*, 2020, **76**, 1–11.

31 Y. Filinchuk, R. Černý and H. Hagemann, *Chem. Mater.*, 2009, **21**, 925–933.

32 Y. Filinchuk, B. Richter, T. R. Jensen, V. Dmitriev, D. Chernyshov and H. Hagemann, *Angew. Chem., Int. Ed.*, 2011, **50**, 11162–11166.

33 W. Lohstroh and M. Heere, *J. Phys. Soc. Jpn.*, 2020, **89**, 051011.

34 B. H. Toby and R. B. Von Dreele, *J. Appl. Crystallogr.*, 2013, **46**, 544–549.

35 J. Chen, Y. S. Chua, H. Wu, Z. Xiong, T. He, W. Zhou, X. Ju, M. Yang, G. Wu and P. Chen, *Int. J. Hydrogen Energy*, 2015, **40**, 412–419.

36 E. Roedern and T. R. Jensen, *ChemistrySelect*, 2016, **1**, 752–755.

37 K. Pu, X. Qu, X. Zhang, J. Hu, C. Gu, Y. Wu, M. Gao, H. Pan and Y. Liu, *Adv. Sci.*, 2019, **6**, 1901776.

38 V. Favre-Nicolin and R. Cerny, *J. Appl. Crystallogr.*, 2002, **35**, 734–743.

39 J. Rodriguez-Carvajal, *Newsletter in Commission on Powder Diffraction (IUCr)*, 2001, **26**, 12–19.

40 P. E. Blöchl, *Phys. Rev. B: Condens. Matter Mater. Phys.*, 1994, **50**, 17953–17979.

41 G. Kresse and J. Furthmüller, *Phys. Rev. B: Condens. Matter Mater. Phys.*, 1996, **54**, 11169–11186.

42 J. P. Perdew, K. Burke and M. Ernzerhof, *Phys. Rev. Lett.*, 1996, **77**, 3865–3868.

43 A. Hammersley, *ESRF Internal Report*, ESRF97HA02T, 1997.

44 V. Dyadkin, P. Pattison, V. Dmitriev and D. Chernyshov, *J. Synchrotron Radiat.*, 2016, **23**, 825–829.

45 D. Chernyshov, V. Dyadkin, W. van Beek and A. Urakawa, *Acta Crystallogr., Sect. A: Found. Adv.*, 2016, **72**, 500–506.

46 Agilent, *CrysAlis PRO*, Agilent Technologies Ltd, Yarnton, Oxfordshire, England, 2014.

47 G. Sheldrick, *Acta Crystallogr., Sect. C: Struct. Chem.*, 2015, **71**, 3–8.

48 M. Heere, M. J. Mühlbauer, A. Schökel, M. Knapp, H. Ehrenberg and A. Senyshyn, *J. Appl. Crystallogr.*, 2018, **51**, 591–595.